Article

Imaging Low-Temperature Phases of Ice with Polarization-Resolved Hyperspectral Stimulated Raman Scattering Microscopy

Published as part of The Journal of Physical Chemistry virtual special issue "Xiaoliang Sunney Xie Festschrift".

Yaxin Chen, Zhijie Liu, and Minbiao Ji*

Read Online

ACCESS | Metrics & More | Article Recommendations | SI Supporting Information

ABSTRACT: Water freezes into various phases of ice under different cryogenic temperatures and pressure conditions, such as ice I_h and ice XI at normal pressure. Vibrational imaging with high spectral, spatial, and polarization resolutions could provide detailed information on ice, including the phases and crystal orientations at the microscopic level. Here, we report in situ stimulated Raman scattering (SRS) imaging of ice to analyze the vibrational spectral changes of the OH stretching modes associated with the phase transition between ice I_h and ice XI. In addition, polarization-resolved measurements were performed to reveal the microcrystal orientations of the two phases of ice, with the spatial-dependent anisotropy pattern indicating the inhomogeneous distribution of their orientations. Furthermore, the angular patterns were theoretically explained by third-order nonlinear optics with the known crystal symmetries of the ice phases. Our work may provide new opportunities to investigate many intriguing physical chemistry properties of ice under low-temperature conditions.
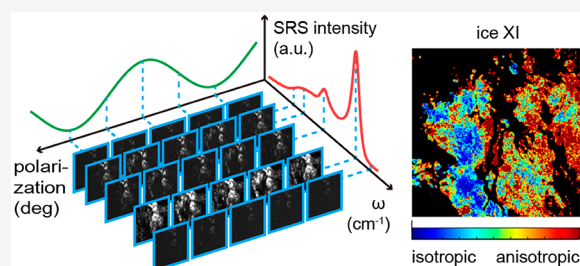
INTRODUCTION

Water is well-known as one of the most important substances on the earth. The dynamic hydrogen bond networks of water ensure its liquid phase under room temperature, while it freezes into solid phases of ice under low temperature and different high-pressure conditions. Ice, with its 20 crystalline and additional amorphous forms,[1] has attracted tremendous research attentions for decades. Natural ice I_h belongs to hexagonal $D_{6h}^4 (P6_3/mcc)$ group, and it transforms into a proton-ordered phase (ice XI) with orthorhombic $C_{2v}^{12}(Cmc2_1)$ symmetry near 70 K.[2,3] In hexagonal ice, the oxygen atoms form the lattice framework while considerable freedom remains for hydrogen atoms to migrate,[4] causing the hydrogen bonds between O and H atoms to form and break randomly and rapidly (within a few picoseconds). In contrast, the low-temperature phase of ice XI was believed to be ferroelectric,[5,6] which was predicted to exhibit hysteresis of dipole orientations.[7] However, other calculations showed that ice XI prefers antiferroelectric in nature.[8,9] The discrepancies may result from the experimental challenges of growing macroscopic single crystal ice XI for spectroscopic measurements, such as sum-frequency vibrational spectroscopy (SFVS),[10] and Raman spectroscopy.[11,12] Therefore, developing new techniques with high spectral and spatial resolutions is vital for studying the physical properties of ice phases and their transitions.

Raman scattering spectroscopy has been a powerful analytical tool to characterize materials by accessing their fingerprint vibrational properties. There are three major

spectral zones in the Raman spectra of water and ice: the translational/librational bands below 400 cm^{-1}, the bending and combination bands at 1100–2400 cm^{-1}, and the stretching modes at 2900–3600 cm^{-1}[12]. Among them, the OH stretching modes were found to be closely related to the phase and structure of ice for revealing the intra- and intermolecular interactions.[13] Moreover, polarization dependent Raman spectra indicated that different vibrational modes exhibited distinct properties with respect to the excitation/detection polarization geometries,[11] which is deeply rooted in the structural symmetry of ice, and offered a means to identify the crystal orientations. In addition to the spectral characteristics of ice, the spatial profiles of ice specimens are also critical to investigate the heterogeneously formed microcrystals with different orientations and phases, especially during low-temperature phase transitions.

However, because of the small scattering cross-section of spontaneous Raman, micro-Raman imaging usually takes hours to generate a high-resolution image in a sample-scanning manner, which has limited its capability in studying the phase transitions of ice. Stimulated Raman scattering (SRS)
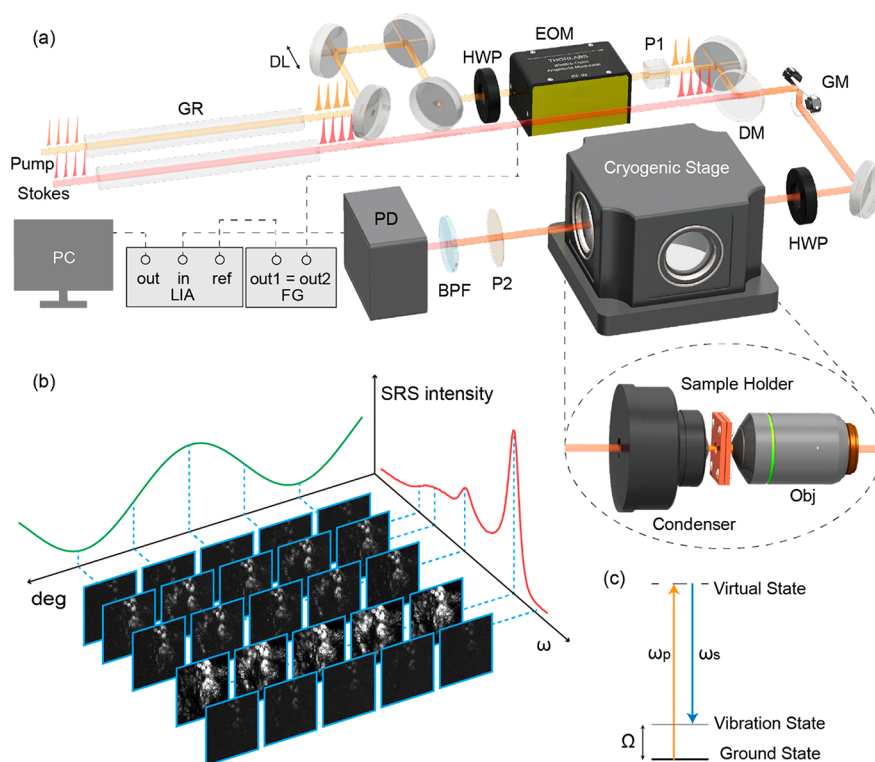
Figure 1. Schematic of the experimental design. (a) Optical layout of the cryogenic SRS microscope. Key: GR, glass rod; DL, delay line; HWP, half-wave plate; EOM, electro-optical modulator; P, polarizer; DM, dichroic mirror; GM, galvo mirror; BPF, band-pass filter; PD, photodiode; LIA, lock-in amplifier; FG, function generator; PC, personal computer. Inset: components inside the cryogenic stage. (b) Four-dimensional hyperspectral image sets with spectral and polarization resolution. (c) Energy diagram of stimulated Raman scattering (SRS) process.

microscopy has been rapidly evolved as a unique chemical imaging modality with $\sim 10^5$ enhancement of Raman signal intensity, while retaining the spectral resolution to realize molecular specific imaging with high speed.[14,15] Exploiting these advantages, SRS microscopy has demonstrated broad applications in many research branches, including label-free tissue histology, lipid metabolism, drug delivery, material sciences, analytical chemistry, environmental sciences, etc.[16−26] Although there have been previous studies of water with coherent Raman scattering (CRS) microscopy,[27−29] imaging ice at low temperatures was seldom reported. Moreover, CRS imaging of crystals with polarization-controlled excitation and polarization-sensitive detections have shown potentials to explore crystal structures and symmetries[30,31]

In this work, we have constructed a cryogenic hyperspectral SRS microscopy system with polarization resolution to access the low-temperature phases of ice I_h and ice XI, and interrogate their crystal orientations. Spectral analysis of the OH stretching bands was applied to extract the symmetric and antisymmetric Raman peaks, which was used to identify ice phases. And the angular anisotropy pattern of SRS intensity was extracted to map out the spatial distribution of the inhomogeneous microcrystal orientations at different phases.

EXPERIMENTAL METHODS

Figure 1a shows the schematic of our home-built cryo-SRS microscopy. A commercial femtosecond optical parametric oscillator (OPO, Insight DS+, Newport Inc.) generated linearly polarized pump (tunable 680−1300 nm, ~150 fs) and Stokes beams (fixed at 1040 nm, ~200 fs). In the spectral focusing mode (Figure S1), the two femtosecond laser beams

were chirped to picoseconds (~3.8 ps for pump pulse and 1.8 ps for Stokes beam) by SF57 glass rods to obtain hyperspectral SRS capability with matched group velocity dispersion (GVD), and the spectral information was acquired by scanning the time delay between the pump and Stokes pulses with a delay line.[32,33] The spatially and temporally overlapped pump and Stokes beams were introduced into a cryogenic stage (Fusion, Montana Instruments) for low-temperature measurements. The two overlapped beams were kept at the same linear polarization by passing through a polarizer. The home-built laser-scanning microscope consisted of a pair of Galvano mirrors (6215H, Cambridge Technology Inc.), a scan lens (SL50-CLS2, Thorlabs), a tube lens (TTL200MP, Thorlabs), an objective lens (Olympus, UPLFLN10XP, NA = 0.3), and a condenser (NA = 1.4, Nikon), where the scan lens and the tube lens formed a 4f system. Under such geometry, the nonresonance background from cross-phase modulation was found to be negligible (Figure S2). The objective lens and the condenser were placed inside the cryostat along with the cooling sample-holder, as shown in the inset of Figure 1a. The SRS process occurred when the pump and Stokes beams interacted with the sample simultaneously at the matched Raman frequency, stimulated Raman loss (SRL) signal was collected by a photodiode (PD) after a bandpass filter (BPF, Chroma, ET890/220M) to pass the pump beam (~780 nm). The Stokes beam was modulated by an electro-optical modulator (EOM, Thorlabs, EO-AM-R-20-C2) at ~20 MHz, and the SRL signal was demodulated by a lock-in amplifier (LIA, Zurich Instruments, HF2LI). The SRS images were then formed using the lock-in output signal and the open-source Scanimage software (MBF Bioscience).[34]
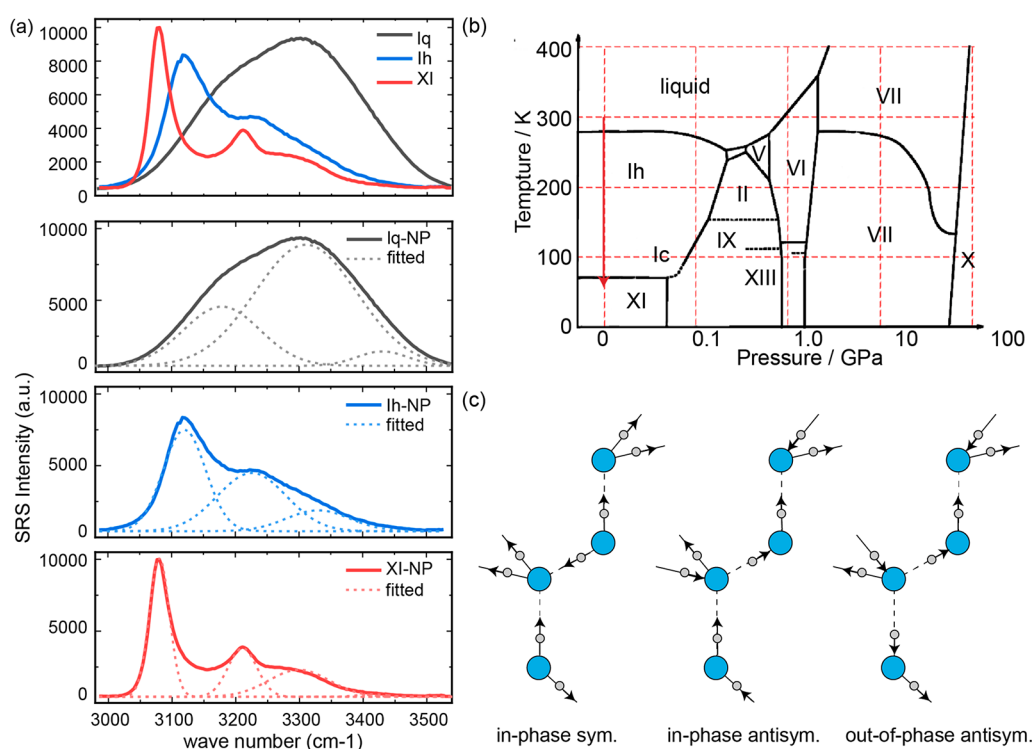
Figure 2. SRS spectra of water and ice. (a) In situ nonpolarized SRS spectra in the region of the OH stretching vibrational modes of liquid water, ice I_h and ice XI. Fitted peak parameters are shown in Table 1. (b) Phase diagram of H_2O, with the cooling path shown in the red arrow. (c) Displacement pattern of symmetric and antisymmetric OH stretching modes. Solid and dashed lines indicate OH bonds and hydrogen bonds, respectively.

To perform polarization-resolved measurements, the two overlapped beams were kept at the same linear polarization, and a broadband achromatic half-wave plate (HWP, AHWP05M-980, Thorlabs) was rotated with an angle φ to control the polarization of the beams (2φ). After the sample and before the PD, an analyzer was rotated by 2φ simultaneously to make sure that the SRS signal was detected in the same polarization as the incident beams. Such a geometry is equivalent to rotating sample perpendicular to the incident laser beams. Therefore, the final polarization- and spectral-resolved image stack form a four-dimensional data $S(x, y, \omega, \varphi)$, as illustrated in Figure 1b. SRS occurs when the energy difference between the pump and Stokes photons is tuned to match the vibrational energy of a particular chemical bond (Figure 1c). As a result, the pump photons are annihilated (stimulated Raman loss, SRL) while the same amount of Stokes photons are generated (stimulated Raman gain, SRG), and the net energy difference is transferred to the excited vibrational states of molecules. In this work, the pump wavelength was chosen from 768 to 788 nm while the Stokes was fixed at 1040 nm to access the SRS spectra of OH stretching modes from ~3000 cm^{-1} to 3500 cm^{-1}. Because of the limited bandwidth of our laser pulses, the spectral focusing mode only cover ~200 cm^{-1} with fixed beam wavelengths. To cover the broad spectral range of OH stretching, spectral stitching was applied with multiple pump center wavelengths (768, 773, 778, 783, and 788 nm). All the spectra were normalized using pure acrylonitrile butadiene styrene (ABS) plastic as reference (Supporting Note S1).

For low temperature measurements, a home-built copper sample holder was used to seal the deionized water at atmospheric pressure, the chamber was a thin well with

diameter Φ = 5 mm and thickness d = 0.2 mm. The sample holder was glued (GE Varnish, CMR direct) to the coldfinger of the cryostat for improved thermal conduction. During the cooling process, the cryo chamber was vacuumed to an ultrahigh vacuum lower than 2 Torr. Water transformed to ice I_h at ~273 K and reached the proton-ordered phase XI below ~70 K. Data were collected at 296 K for liquid water, 180 K for ice I_h, and 15 K for ice XI, and the temperature stability was kept within 25 mK during the measurements.

■ RESULTS AND DISCUSSION

SRS Spectra of Water and Ice. We first measured SRS spectra of liquid water, ice I_h, and ice XI, showing distinct spectral features of the three phases (Figure 2a). The phase diagram of water indicates the cooling pathway from liquid water to ice I_h, and ice XI around atmospheric pressure (Figure 2b). Similar to spontaneous Raman spectra,[12] SRS spectra are superpositions of multiple bands attributed to different OH stretching vibrational modes. To quantitatively analyze these modes, spectral decompositions were conducted by fitting the SRS spectrum of each phase into the sum of multiple Gaussian peaks, as shown in dashed lines in Figure 2b. For liquid water, three vibrational bands centered at 3178, 3430, and 3502 cm^{-1} could be identified. When water underwent phase transition from liquid to ice I_h, all the bands were significantly narrowed and red-shifted to 3120, 3226, and 3330 cm^{-1}. And for ice XI, the bands were further red-shifted to 3080, 3211, and 3300 cm^{-1}. The molecular alignment of ice and the atomic displacements of different OH stretching vibrations are shown in Figure 2c. In ice I_h, H_2O molecules form a hexagonal lattice, while in ice XI H_2O molecules form an orthorhombic lattice. The assignments of these vibrational bands may be a bit

complicated, because of the proton transfer between H_2O molecules (for ice above 5 K) leading to the labile and dynamic hydrogen bond network, as well as the intra- and intermolecule coupling and combination between different stretching modes.[12,35,36] Nevertheless, the lowest-frequency Raman peak of ice was commonly assigned to in-phase symmetric stretch vibration.[37] While the two higher-frequency peaks within $3200-3400$ cm^{-1} were considered to be antisymmetric vibrations,[38] with the in-phase antisymmetric mode centered around 3200 cm^{-1} and the out-phase mode around 3300 cm^{-1}.

An overall red-shift of all the vibrational peaks was observed during the cooling process, which may be attributed to the strengthening of the hydrogen-bonds when water molecules become more fixed in the lattice. Compared with the free OH stretching centered at $\sim$3700 cm^{-1},[39] hydrogen bonding in liquid water tends to lower the frequency to $\sim$3400 cm^{-1}, and the various types and configurations of rapidly exchanging hydrogen bonds result in the heterogeneously broadened peaks in liquid phase.[40-42] When ice forms, the well-orientated molecules in the crystal lattice form stronger hydrogen bonds with much more homogeneous bonding configurations, which thus results in the narrowing and red-shifting of all the vibrational peaks. Such a trend continues when further cooling and phase-transition to ice XI occurs. The peak centers and widths of all the measured O−H stretching modes are summarized in Table 1.

Table 1. Vibrational Frequencies and Peak Widths of the OH Stretching Bands of Liquid Water and Ice I_h and XI

phase	freq (cm^{-1})	fwhm	freq (cm^{-1})	fwhm	freq (cm^{-1})	fwhm
liquid	3178	122.0	3430	160.1	3502	100.5
ice I_h	3120	66.8	3226	108.0	3330	95.6
ice XI	3080	31.5	3211	45.8	3300	80.1
assignment	in-phase sym.		in-phase antisym.		out-of-phase antisym.	

An enhancement in SRS intensity of the lowest-frequency symmetric stretching mode ($\sim$3100 cm^{-1}) and a reduction in intensity of the higher-frequency antisymmetric mode ($\sim$3300 cm^{-1}) were observed during the low-temperature phase transitions. In liquid water, the inhomogeneity and flexibility of the hydrogen-bond networks causing a stronger antisymmetric vibration than the symmetric one.[43] After the formation of ice, the thermal motions of H_2O molecules are largely reduced, causing smaller thermal agitation and the formation of steady structures. The increased symmetry of ice crystals results in strong Raman-active symmetric vibration mode, and reduced Raman scattering cross-section for the antisymmetric mode at low temperatures.[13] The peak narrowing and red-shifting were considered as proper spectral markers of different phases during phase transitions.

Imaging Ice Phase Transitions with SRS. Based on the spectral features of water and ice phases, it is convenient to image the process of phase transitions in situ with SRS. For example, we could focus on imaging the in-phase symmetric OH stretch modes (3120 and 3080 cm^{-1}) during the heating process from ice XI to ice I_h. It is already known that ice XI possesses a narrow and strong peak for this vibrational mode, which tends to blue shift and broaden when the ice phase transforms into ice I_h. Therefore, SRS images recording the

phase transitions for increasing temperatures demonstrated a continuous increase of intensity from 55 to 98 K when imaged at 3120 cm^{-1} (Figure 3a), and a decrease of intensity for 3080
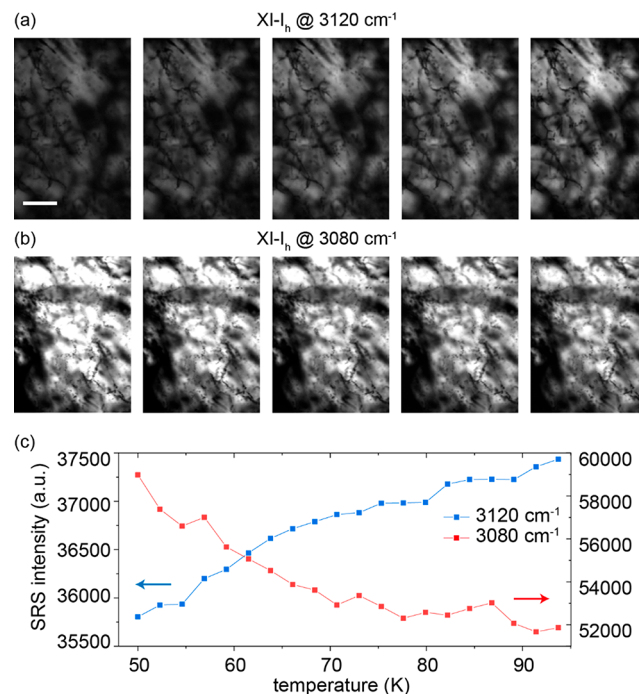

Figure 3. Imaging ice phase transitions with SRS. (a-b) SRS images of the phase transition at symmetric OH stretching modes (a) 3210 cm^{-1} and (b) 3080 cm^{-1} from ice XI to ice I_h during heating process. (c) Temperature dependent SRS intensity during the phase transition. Scale bar: 200 μm.

cm^{-1} (Figure 3b). The temperature-dependent SRS signal of these two Raman frequencies could reveal the process of phase transition from ice XI to ice I_h (Figure 3c). We can also image at different Raman peaks, the phase transition from ice I_h to liquid water could be well resolved at 3210 cm^{-1} to see the increased SRS intensity when ice melted into water, with the melting process successfully taken by the high-speed SRS microscopy (Figure S3). As expected, phase transitions did not occur uniformly across the sample, the spatiotemporal dynamics captured by SRS may provide useful information associated with the physical properties of ice formation, melting, and nucleation.

Polarization-Resolved SRS Imaging of Ice. During our polarization-resolved measurements, the analyzer was synchronized to the rotation of the HWP to keep the detected SRS signal in the same polarization as the pump and Stokes beams. This geometry is equivalent to sample rotation, and the measured SRS signal is related to the induced third-order polarization parallel to the incident light fields. Polarization-resolved SRS images of ice I_h (180 K) at the symmetric stretching band (3120 cm^{-1}) are shown in Figure 4a, and those of ice XI (15 K) at 3080 cm^{-1} are shown in Figure 4b, where 0° was defined as the polarization normal to the optical bench. It can be readily seen that different regions of the sample exhibited different responses to polarization changes. SRS intensity in certain areas (green squares) changed drastically from almost zero to its maximum when the polarization angle was changed from 0° to 45°. In contrast, other regions (orange squares) appeared constant SRS intensity—independent of
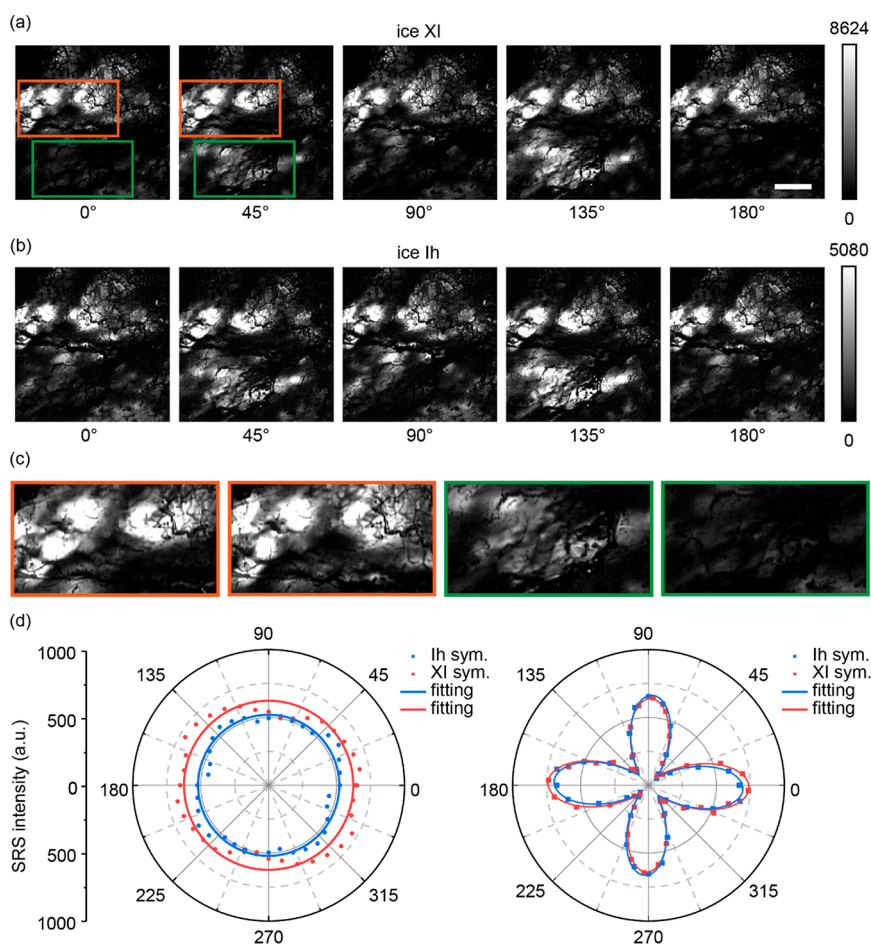
Figure 4. Polarization-resolved SRS imaging of ice I_h and ice XI. (a-b) SRS images at symmetrical stretching (a) 3080 cm^{-1} for ice XI and (b) 3120 cm^{-1} ice I_h. Orange and green squares indicate typical regions with isotropic and 4-fold polarization responses. (c) Zoomed-in image of the two typical regions. (d) Azimuthal angular dependent SRS patterns of ice I_h and ice XI in the two typical regions. SRS data and fitting results are shown in blue and red for ice I_h and ice XI, respectively. Scale bar: 200 μm.

polarization angle. The magnified images of the two representative areas are shown in Figure 4c. Consequently, SRS signal exhibiting isotropic or 4-fold angular pattern with respect to incident polarization could be clearly measured (Figure 4d), and the theoretical explanations shown in the later text were used to fit the experimental data. Despite of the two special anisotropy patterns, a superposition of 4-fold, 2-fold, and a constant polarization response was observed. It may come from the interference between microcrystals or the inclination between the special crystal orientation and the incident beam. Comparing the angular pattern between the two ice phases, it could be found that the polarization dependence kept unchanged when phase transition occurred between ice I_h and ice XI. This indicates crystal orientation remains stable during solid−solid phase transition, in contrary to the phase transition to liquid where the polarization dependence becomes isotropic (Figure S4), just as expected. These results implied that the angular pattern of polarization-resolved SRS may be used to represent microcrystal orientations for ice I_h and ice XI.

Similar features of the ice phases were observed in the antisymmetric bands (Figure S5). Although it is known that the dipole orientations of the symmetric and antisymmetric OH stretch modes are different, the measured polarization dependences of both modes appear almost identical. Particularly, the 4-fold angular pattern remain the same for the symmetric and antisymmetric vibrations. This could be understood by the fact that the symmetric and antisymmetric stretching dipoles of H_2O molecule are orthogonal to each other, hence the angular pattern of the 4-fold symmetry remain unchanged by a 90° rotation. And for the isotropic pattern, the symmetry obviously preserves for both modes.

Theoretical Interpretation of SRS Polarization-Dependence for Ice Crystals. The SRS response is encoded in the $\chi^{(3)}$ for the third-order nonlinear optical process of SRS. In SRL, we measured $\chi_R(\omega_p) = \chi^{(3)}(\omega_p; -\omega_s, \omega_s)$, where $\chi^{(3)}$ is the third-order susceptibility in crystal coordinate, and ω_p and ω_S are the frequencies of the pump and Stokes, respectively. The third-order nonlinear polarization reads:

$$P^{(3)}(\omega_p) = \frac{\varepsilon_0 D}{4} \chi_{lab}^{(3)}(\omega_p; \omega_p, -\omega_s, \omega_s) E_S E_S^* E_p \qquad (1)$$

where $D = 3$ for $\omega_0 = \omega_p$ or ω_s, $\chi_{lab}^{(3)}$ is the third-order susceptibility in lab coordinate, which can be transformed from that of the crystal coordinate $\chi_{cry, pqrs}^{(3)}$ through Euler's rotation R,

$$\chi_{lab,ijkl}^{(3)} = \sum_{pqrs} \chi_{cry,pqrs}^{(3)} R_{lp} R_{jq} R_{kr} R_{ls} \qquad (2)$$

where $i, j, k, l \in \{x, y, z\}$, stand for the lab coordinate; and $p, q, r, s \in \{a,b,c\}$, stand for the crystal coordinate. In our
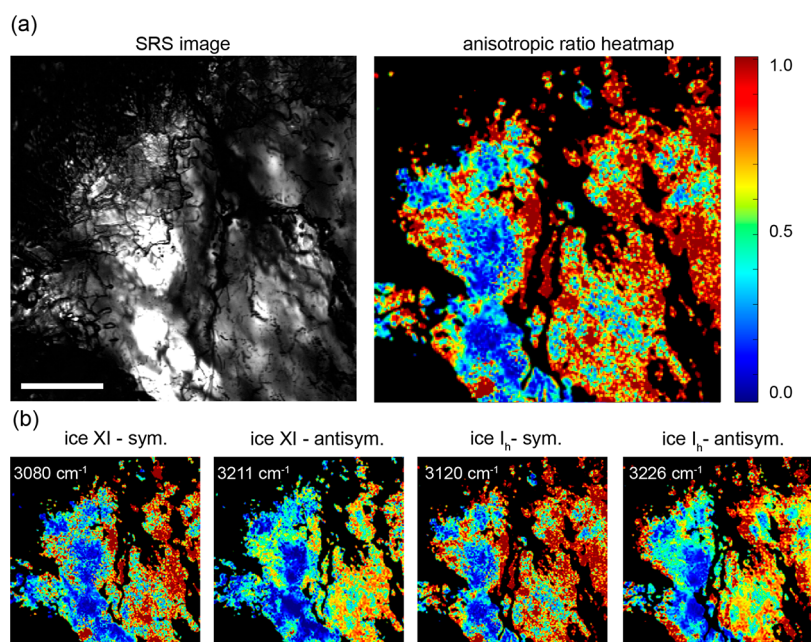
(a)

(b)

Figure 5. Heatmap of the anisotropy ratio extracted from polarization-resolved SRS. (a) SRS image of symmetrical stretching band of ice XI and the corresponding anisotropy ratio heatmap. (b) Spatial distribution of the anisotropy ratio in ice I_h and ice XI for different vibrational modes. Scale bar: 200 μm.

polarization-resolved measurement, the polarization direction of the pump beam is the same as the Stokes beam; hence, the third-order signal field reads,

$$E_p^{(3)} = i\chi_{lab,1111}^{(3)} E_S E_S^* E_p \quad (3)$$

The SRL signal represents the heterodyne-detected interference between the signal field $E_p^{(3)}$ and the "local oscillator"—the pump field E_p,[44]

$$S_{SRL} = \text{Im}[\chi_{lab,1111}^{(3)}] I_p I_S \quad (4)$$

Note that ice I_h belongs to hexagonal $D_{6h}^4 (P6_3/mcc)$ group, there are 10 independent nonzero third-order susceptibility elements,[45]

$zzzz, xxxx = yyyy = xxyy + xyyx + xyxy, xxyy$

$= yyxx, xyyx = yxxy, xyxy = yxyx, yyzz = xxzz, zzyy$

$= zzxx, zyyz = zxxz, yzzy = xzzx, yzyz = xzxz, zyzy$

$= zxzx \quad (5)$

For the case where the incident beams are normal to the (0001) surface of ice I_h, the SRS intensity remains constant (Supporting Note S2), corresponding to the isotropic pattern,

$$S_{SRL} \propto \text{Im}[\chi_{lab,1111}^{(3)}] \propto \text{Im}[\chi_{xxxx}] \quad (6)$$

Consider another geometry where the incident beams are normal to the $(1\bar{2}10)$ surface of ice I_h, the SRS angular dependence could be deduced to a 4-fold symmetry (Supporting Note S2) as

$$S_{SRL} \propto \text{Im}[\chi_{lab,1111}^{(3)}]$$

$$\propto \text{Im}[\chi_{xxxx} \cos x^4 \varphi + (\chi_{sum})\cos^2\varphi \sin^2\varphi + \chi_{zzzz} \sin^4\varphi] \quad (7)$$

where $\chi_{sum} = \chi_{yyzz} + \chi_{zzyy} + \chi_{zyyz} + \chi_{yzzy} + \chi_{yzyz} + \chi_{zyzy}$.

Ice XI belongs to orthorhombic $C_{2v}^{12}(Cmc2_1)$ group, with 21 nonzero elements with the same subscript indexes as ice I_h. The polarization dependences of ice XI yield the same results as ice I_h following similar theoretical deductions. Therefore, in our analysis the isotropic part was fitted to a constant and the anisotropic part was fitted to eq 7. The rotational angular pattern allows us to determine the orientations of microcrystals in ice.

Anisotropy Distribution Extracted from Polarization-Resolved SRS. As we mentioned, SRS angular pattern with distinct symmetry features (e.g., isotropic and 4-fold) indicates regions with higher symmetry that are more suitable for further investigation. We derived the isotropic and anisotropic parts from the angular pattern of SRS signal, and map out the normalized anisotropic ratio as shown in Figure 5. The larger ratio indicates a higher degree of anisotropy, as shown in red, while a lower degree of anisotropy was shown in blue. By varying the polarization of the incident pump and Stokes beams, 19 SRS images at different polarization angles (from 0 to 180°) were obtained. And the polarization-dependent SRS intensity at each pixel was fitted to a superposition of a constant for the isotropic part (S_{iso}) and a 4-fold angular function (S_{aniso}) for the anisotropic part. After the pixel-by-pixel analysis, a mapping of the S_{aniso}/S_{iso} ratio could be acquired, revealing the spatial distribution of crystal orientation. In contrast to the intensity map of the ice sample, the isotropic ratio map reports the spatial distribution of crystal orientation that is not correlated to the intensity distribution. Figure 5b shows the anisotropy maps of both symmetric and antisymmetric OH stretching modes for both ice I_h and XI. The results indicate that the anisotropy distribution is independent of the vibrational mode, as expected from the above angular pattern results. In addition, ice I_h and ice XI exhibited similar distribution of anisotropy, indicating that the crystal orientations tend to preserve during solid−solid phase transitions. These results demonstrate that the degree of

anisotropy of ice I_h may serve as an indicator of the quality of ice XI in advance, before the occurrence of phase transition.

There remain challenges to extract accurate crystal structural information with polarization-resolved SRS. In particular, this is true for the isotropic angular pattern, which may be possibly due to the amorphous phase of ice, in addition to the crystal orientation mentioned above. In contrast, strong anisotropy of the 4-fold angular pattern would infer high quality crystallization oriented in the special direction ($1\bar{2}10$). Therefore, improving sample qualities to enable the formation of microcrystals with decent size ($>\mu$m) is critical for determining the detailed orientational information, as well as its spatial distribution. Future work may be more focused on the relationship between crystal order and SRS spectra, e.g., the spectral broadening and shifting associated with the degrees of crystallization/amorphousness. Moreover, different vibrational modes and dipole orientations may be studied by introducing isotope diluted H_2O/D_2O to provide more complete pictures of the spectral and structural properties during low-temperature phase transitions of ice.

CONCLUSIONS

To summarize, we have demonstrated in situ hyperspectral SRS imaging of ice with both spectral and polarization resolutions. The red-shifting and narrowing of the SRS spectra were observed when water transformed from of liquid to ice I_h and ice XI under low-temperature phase transitions, enabling convenient optical differentiation of these phases. Furthermore, the polarization dependence of SRS signal for ice I_h and ice XI were analyzed to reflect the crystal symmetries and orientations, as well as their spatial inhomogeneity within the sample. Our method provides potentials to investigate new physical chemistry properties of ice under extreme conditions.

ASSOCIATED CONTENT

⑤I Supporting Information

The Supporting Information is available free of charge at https://pubs.acs.org/doi/10.1021/acs.jpcb.2c09068.

> Figure S1, schematic of spectral focusing; Figure S2, SRS image during the phase transition from ice I_h to liquid water; Figure S3, polarization-dependent SRS analysis of liquid water; Figure S4, polarization-resolved SRS images of ice I_h and ice XI; Note S1, stitching method of SRS spectra; and Note S2, theoretical interpretation of polarization-resolved SRS pattern (PDF)

AUTHOR INFORMATION

Corresponding Author

Minbiao Ji − *State Key Laboratory of Surface Physics and Department of Physics, Human Phenome Institute, Academy for Engineering and Technology, Key Laboratory of Micro and Nano Photonic Structures (Ministry of Education), Fudan University, Shanghai 200433, China; Yiwu Research Institute of Fudan University, Yiwu City, Zhejiang 322000, China;* ⓞ orcid.org/0000-0002-9066-4008; Email: minbiaoj@fudan.edu.cn

Authors

Yaxin Chen − *State Key Laboratory of Surface Physics and Department of Physics, Human Phenome Institute, Academy for Engineering and Technology, Key Laboratory of Micro*

and Nano Photonic Structures (Ministry of Education), Fudan University, Shanghai 200433, China

Zhijie Liu − *State Key Laboratory of Surface Physics and Department of Physics, Human Phenome Institute, Academy for Engineering and Technology, Key Laboratory of Micro and Nano Photonic Structures (Ministry of Education), Fudan University, Shanghai 200433, China*

Complete contact information is available at:
https://pubs.acs.org/10.1021/acs.jpcb.2c09068

Author Contributions

M. Ji conceived the work. Y. Chen performed SRS measurements and data analysis. Y. Chen and M. Ji wrote the manuscript together.

Notes

The authors declare no competing financial interest.

REFERENCES

(1) Hansen, T. C. The Everlasting Hunt for New Ice Phases. *Nat. Commun.* **2021**, *12* (1), 3161.

(2) Tajima, Y.; Matsuo, T.; Suga, H. Phase Transition in KOH-Doped Hexagonal Ice. *Nature* **1982**, *299* (5886), 810−812.

(3) Howe, R.; Whitworth, R. W. A Determination of the Crystal Structure of Ice XI. *J. Chem. Phys.* **1989**, *90*, 4450.

(4) Bove, L. E.; Klotz, S.; Paciaroni, A.; Sacchetti, F. Anomalous Proton Dynamics in Ice at Low Temperatures. *Phys. Rev. Lett.* **2009**, *103* (16), 165901.

(5) Iedema, M. J.; Dresser, M. J.; Doering, D. L.; Rowland, J. B.; Hess, W. P.; Tsekouras, A. A.; Cowin, J. P. Ferroelectricity in Water Ice. *J. Phys. Chem. B* **1998**, *102* (46), 9203−9214.

(6) Fukazawa, H.; Hoshikawa, A.; Ishii, Y.; Chakoumakos, B. C.; Fernandez-Baca, J. A. EXISTENCE OF FERROELECTRIC ICE IN THE UNIVERSE. *ApJ* **2006**, *652*, L57.

(7) Zhao, W.-H.; Bai, J.; Yuan, L.-F.; Yang, J.; Zeng, X. C. Ferroelectric Hexagonal and Rhombic Monolayer Ice Phases. *Chemical Science* **2014**, *5* (5), 1757−1764.

(8) Parkkinen, P.; Riikonen, S.; Halonen, L. Ice XI: Not That Ferroelectric. *J. Phys. Chem. C* **2014**, *118* (45), 26264−26275.

(9) Tribello, G. A.; Slater, B. Proton Ordering Energetics in Ice Phases. *Chem. Phys. Lett.* **2006**, *425* (4), 246−250.

(10) Su, X.; Lianos, L.; Shen, Y. R.; Somorjai, G. A. Surface-Induced Ferroelectric Ice on Pt(111). *PHYSICAL REVIEW LETTERS* **1998**, *80* (7), 1533.

(11) Abe, K.; Shigenari, T. Raman Spectra of Proton Ordered Phase XI of ICE I. Translational Vibrations below 350 Cm $^{-1}$. *J. Chem. Phys.* **2011**, *134* (10), 104506.

(12) Shigenari, T.; Abe, K. Vibrational Modes of Hydrogens in the Proton Ordered Phase XI of Ice: Raman Spectra above 400 Cm−1. *J. Chem. Phys.* **2012**, *136*, 174504.

(13) Đurickovic, I.; Claverie, R.; Bourson, P.; Marchetti, M.; Chassot, J.-M.; Fontana, M. D. Water−Ice Phase Transition Probed by Raman Spectroscopy. *J. Raman Spectrosc.* **2011**, *42* (6), 1408−1412.

(14) Freudiger, C. W.; Min, W.; Saar, B. G.; Lu, S.; Holtom, G. R.; He, C.; Tsai, J. C.; Kang, J. X.; Xie, X. S. Label-Free Biomedical Imaging with High Sensitivity by Stimulated Raman Scattering Microscopy. *Science* **2008**, *322* (5909), 1857−1861.

(15) Nandakumar, P.; Kovalev, A.; Volkmer, A. Vibrational Imaging Based on Stimulated Raman Scattering Microscopy. *New J. Phys.* **2009**, *11* (3), 033026.

(16) Hu, F.; Shi, L.; Min, W. Biological Imaging of Chemical Bonds by Stimulated Raman Scattering Microscopy. *Nat. Methods* **2019**, *16* (9), 830−842.

(17) Manifold, B.; Fu, D. Quantitative Stimulated Raman Scattering Microscopy: Promises and Pitfalls. *Annual Review of Analytical Chemistry* **2022**, *15* (1), 269−289.

(18) Cheng, Q.; Miao, Y.; Wild, J.; Min, W.; Yang, Y. Emerging Applications of Stimulated Raman Scattering Microscopy in Materials Science. *Matter* **2021**, *4* (5), 1460−1483.

(19) Miao, X.; Zhang, G.; Wang, F.; Yan, H.; Ji, M. Layer-Dependent Ultrafast Carrier and Coherent Phonon Dynamics in Black Phosphorus. *Nano Lett.* **2018**, *18* (5), 3053−3059.

(20) Ao, J.; Feng, Y.; Wu, S.; Wang, T.; Ling, J.; Zhang, L.; Ji, M. Rapid, 3D Chemical Profiling of Individual Atmospheric Aerosols with Stimulated Raman Scattering Microscopy. *Small. Methods* **2020**, *4* (2), 1900600.

(21) Yang, Y.; Yang, Y.; Liu, Z.; Guo, L.; Li, S.; Sun, X.; Shao, Z.; Ji, M. Microcalcification-Based Tumor Malignancy Evaluation in Fresh Breast Biopsies with Hyperspectral Stimulated Raman Scattering. *Anal. Chem.* **2021**, *93*, 6223.

(22) Zhang, C.; Li, J.; Lan, L.; Cheng, J.-X. Quantification of Lipid Metabolism in Living Cells through the Dynamics of Lipid Droplets Measured by Stimulated Raman Scattering Imaging. *Anal. Chem.* **2017**, *89* (8), 4502−4507.

(23) Saar, B. G.; Contreras-Rojas, L. R.; Xie, X. S.; Guy, R. H. Imaging Drug Delivery to Skin with Stimulated Raman Scattering Microscopy. *Mol. Pharmaceutics* **2011**, *8* (3), 969−975.

(24) Ling, J.; Miao, X.; Sun, Y.; Feng, Y.; Zhang, L.; Sun, Z.; Ji, M. Vibrational Imaging and Quantification of Two-Dimensional Hexagonal Boron Nitride with Stimulated Raman Scattering. *ACS Nano* **2019**, *13* (12), 14033−14040.

(25) Liu, Z.; Su, W.; Ao, J.; Wang, M.; Jiang, Q.; He, J.; Gao, H.; Lei, S.; Nie, J.; Yan, X.; Guo, X.; Zhou, P.; Hu, H.; Ji, M. Instant Diagnosis of Gastroscopic Biopsy via Deep-Learned Single-Shot Femtosecond Stimulated Raman Histology. *Nat. Commun.* **2022**, *13* (1), 4050.

(26) Ao, J.; Fang, X.; Miao, X.; Ling, J.; Kang, H.; Park, S.; Wu, C.; Ji, M. Switchable Stimulated Raman Scattering Microscopy with Photochromic Vibrational Probes. *Nat. Commun.* **2021**, *12* (1), 3089.

(27) Figueroa, B.; Hu, R.; Rayner, S. G.; Zheng, Y.; Fu, D. Real-Time Microscale Temperature Imaging by Stimulated Raman Scattering. *J. Phys. Chem. Lett.* **2020**, *11* (17), 7083−7089.

(28) Zhu, H.; Li, Y.; Vdović, S.; Long, S.; He, G.; Guo, Q. Femtosecond Coherent Anti-Stokes Raman Scattering Spectroscopy of Hydrogen Bonded Structure in Water and Aqueous Solutions. *Spectrochimica Acta Part A: Molecular and Biomolecular Spectroscopy* **2015**, *151*, 262−273.

(29) Li, T.; Li, F.; Li, Z.; Sun, C.; Tong, J.; Fang, W.; Men, Z. Influence of Strong and Weak Hydrogen Bonds in Ices on Stimulated Raman Scattering. *Opt. Lett.* **2016**, *41* (6), 1297.

(30) Cleff, C.; Gasecka, A.; Ferrand, P.; Rigneault, H.; Brasselet, S.; Duboisset, J. Direct Imaging of Molecular Symmetry by Coherent Anti-Stokes Raman Scattering. *Nat. Commun.* **2016**, *7* (1), 1−7.

(31) Suhalim, J. L.; Chung, C.-Y.; Lilledahl, M. B.; Lim, R. S.; Levi, M.; Tromberg, B. J.; Potma, E. O. Characterization of Cholesterol Crystals in Atherosclerotic Plaques Using Stimulated Raman Scattering and Second-Harmonic Generation Microscopy. *Biophys. J.* **2012**, *102* (8), 1988−1995.

(32) Fu, D.; Holtom, G.; Freudiger, C.; Zhang, X.; Xie, X. S. Hyperspectral Imaging with Stimulated Raman Scattering by Chirped Femtosecond Lasers. *J. Phys. Chem. B* **2013**, *117* (16), 4634−4640.

(33) He, R.; Xu, Y.; Zhang, L.; Ma, S.; Wang, X.; Ye, D.; Ji, M. Dual-Phase Stimulated Raman Scattering Microscopy for Real-Time Two-Color Imaging. *Optica* **2017**, *4* (1), 44.

(34) Pologruto, T. A.; Sabatini, B. L.; Svoboda, K. ScanImage: Flexible Software for Operating Laser Scanning Microscopes. *Biomed. Eng. Online* **2003**, *2*, 13.

(35) Devlin, J. P.; Wooldridge, P. J.; Ritzhaupt, G. Decoupled Isotopomer Vibrational Frequencies in Cubic Ice: A Simple Unified View of the Fermi Diads of Decoupled H2O, HOD, and D2O. *J. Chem. Phys.* **1986**, *84* (11), 6095.

(36) Sivakumar, T. C.; Rice, S. A.; Sceats, M. G. Raman Spectroscopic Studies of the OH Stretching Region of Low Density Amorphous Solid Water and of Polycrystalline Ice Ih. *J. Chem. Phys.* **1978**, *69* (8), 3468−3476.

(37) McGraw, R.; Madden, W. G.; Bergren, M. S.; et al. A Theoretical Study of the OH Stretching Region of the Vibrational Spectrum of Ice Ih. *The Journal of Chemical Physics* **1978**, *69*, 3483.

(38) Devlin, J. P. Polarized Raman Spectra for the Full Range of Isotopic Dilution for Ice I $_c$ and Amorphous Ice: Mixtures of Intact H $_2$ O and D $_2$ O. *J. Chem. Phys.* **1989**, *90* (3), 1322−1329.

(39) Miyazaki, M.; Fujii, A.; Ebata, T.; Mikami, N. Infrared Spectroscopic Evidence for Protonated Water Clusters Forming Nanoscale Cages. *Science* **2004**, *304*, 1134.

(40) Ji, M.; Odelius, M.; Gaffney, K. J. Large Angular Jump Mechanism Observed for Hydrogen Bond Exchange in Aqueous Perchlorate Solution. *Science* **2010**, *328* (5981), 1003−1005.

(41) Ramasesha, K.; Roberts, S. T.; Nicodemus, R. A.; Mandal, A.; Tokmakoff, A. Ultrafast 2D IR Anisotropy of Water Reveals Reorientation during Hydrogen-Bond Switching. *J. Chem. Phys.* **2011**, *135* (5), 054509.

(42) Perakis, F.; De Marco, L.; Shalit, A.; Tang, F.; Kann, Z. R.; Kühne, T. D.; Torre, R.; Bonn, M.; Nagata, Y. Vibrational Spectroscopy and Dynamics of Water. *Chem. Rev.* **2016**, *116* (13), 7590−7607.

(43) Kühne, T. D.; Khaliullin, R. Z. Nature of the Asymmetry in the Hydrogen-Bond Networks of Hexagonal Ice and Liquid Water. *J. Am. Chem. Soc.* **2014**, *136* (9), 3395−3399.

(44) Dong, P.-T.; Zong, C.; Dagher, Z.; Hui, J.; Li, J.; Zhan, Y.; Zhang, M.; Mansour, M. K.; Cheng, J.-X. Polarization-Sensitive Stimulated Raman Scattering Imaging Resolves Amphotericin B Orientation in Candida Membrane. *Science Advances* **2021**, *7* (2), eabd5230.

(45) Boyd, R. *Nonlinear Optics*, 3rd ed.; NONLINEAR OPTICS: 2008; p 613.